J Mater Sci (2009) 44:6608–6616
DOI 10.1007/s10853-009-3575-8

MESOSTRUCTURED MATERIALS

Construction and characterization of tunable meso-/macroporous tungsten oxide-based transmissive electrochromic devices

Subramanian Balaji · Yahia Djaoued · André-Sébastien Albert · Richard Z. Ferguson · Ralf Brüning · Bao-Lian Su

Received: 29 November 2008 / Accepted: 12 May 2009 / Published online: 28 May 2009

Abstract Recent developments in the processing of porous transition metal oxide thin films have opened up new opportunities in the construction of electrochromic (EC) devices with enhanced properties. Tungsten oxide (WO_3) is one of the most promising materials for EC devices. In this work, we report on the synthesis of meso-/macroporous WO_3 thin films using tungstic acid as precursor and organically modified silane (ORMOSIL) as a templating agent. Calcination of the film at 500 °C resulted in nanocrystalline monoclinic tungsten oxide (m-WO_3) with crystallite sizes of $\sim$16 nm. The meso-/macroporous structure is retained after calcination. An asymmetric EC device based on the meso-/macroporous m-WO_3 thin film was constructed. Thus constructed EC device was characterized by micro-Raman spectroscopy, scanning electron microscopy, transmission electron microscopy, and X-ray diffraction (XRD). Detailed micro-Raman and XRD studies of the intercalation and deintercalation of lithium (Li) in the meso-/macroporous m-WO_3 layer of the EC device as a function of the applied voltage were performed. The meso-/macroporous WO_3 layer, which was found to be monoclinic before Li intercalation, transforms to its higher symmetric phase of tetragonal and toward cubic phase when Li is intercalated into it. Upon complete deintercalation, these phase transitions were reversed and m-WO_3 is recovered. Optical transmission studies were performed in conjunction with Raman and XRD studies. This study shows that meso-/macroporous m-WO_3 layer-based EC device exhibit a high color contrast during the coloration and bleaching.

S. Balaji · Y. Djaoued (✉) · A.-S. Albert · R. Z. Ferguson
Laboratoire de Micro-Spectroscopies Raman et FTIR, Université de Moncton – Campus de Shippagan, 218, boul. J.-D. Gauthier, Shippagan, NB E8S 1P6, Canada
e-mail: djaoued@umcs.ca

R. Brüning
Physics Department, Mount Allison University, 63B York St., Sackville, NB E4L 1G7, Canada

B.-L. Su
Laboratoire de Chimie des Matériaux Inorganiques, The University of Namur (FUNDP), 61 Rue de Bruxelles, 5000 Namur, Belgium

Introduction

Electrochromic (EC) materials undergo reversible optical modulations when intercalated with cations such as H^+, Li^+, etc. Tungsten oxide is an important cathodic inorganic EC material as it exhibits interesting EC properties in its amorphous, nanocrystalline as well as in crystalline forms. WO_3 as an electrochromically active layer find applications in EC displays, as a solar energy material in smart windows, light dimming helmet visors, electronic papers, read-write optical memory devices, etc [1–6].

A typical asymmetric transmissive EC device consists of an ion conducting layer (ICL) (which also acts as a counter electrode) and a WO_3 EC layer as the working cathode, sandwiched between two transparent conductive electrodes. When a small voltage (1.0–3.0 V) is applied across the transparent conductors, ions move from the counter electrode and electrons from the transparent electrode to the EC layer to trigger a color change. Depending upon the amount of intercalated cations, a visible optical change is observed, due to the generation of visible region electronic absorption bands in the EC layer. This phenomenon termed as electrochromism, can be represented as:

$$\underset{\text{Clear}}{WO_3} + xLi^+ + xe^- \leftrightarrow \underset{\text{Dark blue}}{Li_xWO_3}$$

where x is the number of electrons (e^-) and lithium ions (Li^+) inserted (ejected) into (out of) the system. Reversing the voltage restores the device to its previous clear (bleached) optical state. Such EC reactions have been performed on the devices having WO_3 as the switchable EC layer [1–4].

WO_3 has been widely synthesized and very well characterized. Various methods have been adopted to synthesize WO_3 thin films, ranging from conventional physical vapor deposition techniques to mild chemical approaches such as sol–gel methods [1–4, 7–12]. The sol–gel process allows a detailed control of the film texture and structure, thus leading to tailored EC properties. Mesoporous WO_3 films prepared by a sol–gel method with block copolymer templates have been investigated by Cheng et al. [13] and by Djaoued et al. [9]. Macroporous WO_3 films were also synthesized by sol–gel technique using polyethylene glycol as a templating agent [10]. The mesoporous materials, due to their higher surface area, exhibit better kinetics for coloration and bleaching in comparison with standard sol–gel-derived WO_3 thin films [13]. On the other hand, macroporous WO_3, which could be useful in a wider range of applications (especially as an ion inserting material), has displayed coloration efficiency values higher than those previously reported in literature [10]. In this scenario, synthesis of meso-/macroporous WO_3 gains importance, where the advantage of high EC efficiency as well as the enhanced charge transporting properties can be achieved in unison.

The properties of WO_3 films such as crystallinity, crystallite sizes, microstructure, porosity, and thickness strongly influence their applicability in EC devices. The crystalline structure of WO_3 is closely related to the structure of Rhenium oxide. X-ray diffraction (XRD) and Raman spectroscopy studies have been performed on the various crystalline phases of tungsten oxide, such as monoclinic, hexagonal, triclinic, and orthorhombic WO_3 [14–16]. This was feasible as these two characterization tools, XRD and Raman spectroscopy, are sensitive to the various crystallographic phases of WO_3. Another interesting aspect is the phase changes that are associated with the EC effect on crystalline WO_3. Intercalation of Li into ReO_3-type tungsten oxides have resulted in the transformation of lower symmetry phases to the higher symmetry phases [7, 17–21]. This intercalation has been widely studied by electrochemical methods [1–4], whereas the phase changes in the WO_3 as a function of the amount of the intercalated lithium has been studied either by Raman spectroscopy or by XRD [17–21]. When both the techniques are employed simultaneously, a detailed study of the intermediate structural changes in the Li_xWO_3 can be performed. These methods of characterization are more practical for the devices as it can be performed nondestructively and they can probe the structural changes occurring in the EC layer and provide an estimation of the quantity of intercalated ions.

In this work, we present a method to prepare meso-/macroporous monoclinic WO_3 films on indium tin oxide (ITO) substrate by using organically modified silicate (ORMOSIL) as template. Meso-/macroporous features of the monoclinic WO_3 films were studied by scanning electron microscopy (SEM), transmission electron microscopy (TEM), and nitrogen absorption-desorption isotherm measurements. An EC device was constructed based on the meso-/macroporous m-WO_3 film. Detailed micro-Raman and XRD studies of the structural changes occurring during the intercalation or deintercalation of Li ions in the meso-/macroporous m-WO_3 layer of the operating EC device as a function of applied voltages were performed. These studies have been performed in conjunction with the optical properties of the device.

Experimental details

Preparation of coating solutions and WO_3 thin films

The sol–gel coating solutions used for the film coating were prepared in accordance with the procedures described in [7]. All the chemicals were used as purchased. The hybrid ORMOSIL used as templating agent was prepared by an acylation reaction involving, poly(propylene glycol)bis(2-aminopropyl ether) (2-APPG) (Aldrich) and isocyanatopropyltriethoxysilane (ICS) (95%, Aldrich) in tetrahydrofuran (THF) (≥99%, Sigma-Aldrich) in the volume ratio 1:0.1:1. This solution was refluxed for 6 h at 65 °C. After this step, THF was removed from the solution. The final solution was transparent and thick.

Tungstic acid solution was prepared by dissolving W powder (Aldrich, 99.9%) in 35% hydrogen peroxide (Ferris). After adding a small amount of anhydrous ethanol (Commercial Alcohols Inc.), the resulting solution was refluxed for 4 h at 80 °C. 1.5 g of hybrid ORMOSIL dissolved in 15 mL of ethanol was added to the refluxed solution and stirred for 1 h. The final solution was used for the WO_3 film coating. The WO_3 films were deposited by dip-coating on SiO_2-coated glass or ITO-coated glass substrates (Sigma-Aldrich), with a surface resistivity 5–15 Ω/sq, at a controlled speed of 4 mm/s. The films were first dried at 80 °C for 2 min and then calcined at 500 °C at a rate of 1 °C/min for 1 h.

The ion conducting (IC) solution was synthesized by adding an alcoholic solution of lithium iodide (LiI)

(Aldrich powder, 99.9%) + iodine (I_2) (BDH, 99.8%, AR) to the hybrid ORMOSIlL. The final solution was viscous with a yellow/brown color [22].

Construction of EC device

EC devices were constructed using meso-/macroporous m-WO_3 films with the configuration ITO-coated glass-1/m-WO_3 layer/ICL/ITO-coated glass-2, where the ITO-coated glass slides are the two transparent electrodes used to apply the electric field, m-WO_3-TiO_2 is the EC layer, and ICL is the ion conducting and electronically insulating layer. On the ITO-coated-glass-1, a WO_3 film was deposited by dip-coating. The films were heated in air at 500 °C for 1 h. The ICL is applied on top of the WO_3 layer and the ITO-coated-glass-2 is gently pressed against this coating to ensure a uniform distribution of the ICL. After making the electrical connections, the EC device is ready for testing. The area of the EC devices was 5 × 2.5 cm^2.

Structural and optical characterization

For SEM characterization of WO_3 layers as well as the EC devices, specimen cross-sections were prepared and mounted vertically on 32 mm diameter aluminum specimen supports with conductive copper tape and colloidal graphite. Specimens were coated with ca. 150 nm gold in a Hummer 6.2 sputtering unit (Anatech Ltd., Hayward, CA) and examined using a JEOL JSM-5600 SEM (JEOL USA, Peabody, MA). Images were collected using an accelerating voltage of 10 kV and at a working distance of 20 mm. TEM of the WO_3 layers were preformed on a small amount of film scrapped off the SiO_2-coated glass substrate and placed into a glass vial. Ethanol was added and the solution was sonicated for 10 min. A drop of the solution was placed on a carbon-coated, 200-mesh copper grid and left to dry overnight. The sample was imaged using a 2011 JEOL STEM at 200 keV. Images were captured on a 4 k × 4 k multiscan CCD camera using Digital Micrograph from Gatan. Nitrogen adsorption and desorption isotherms were obtained on a Micromeritics Tristar 3000 system at liquid nitrogen temperature. A thick WO_3 layer was deposited by dip-coating on SiO_2-coated glass substrate and subsequently annealed in air at 500 °C for 1 h. The film was scrapped off the substrate and used for measurements. The sample was degassed at 80 °C overnight before measurements were made. The specific surface area was determined by the Brunauer–Emmett–Teller (BET) method, and the pore size distribution was obtained from the N_2 adsorption branch of the isotherms using the Barett–Joyner–Halenda (BJH) method. The crystal structure changes of the Li_xWO_3 layer in an operating EC device as a function of the applied voltage ranging from 1.0 to 2.5 V were studied by micro-Raman spectroscopy. The individual layers used in the fabrication of the EC device were also characterized. Raman spectra were recorded at room temperature with a Jobin-Yvon Labram HR microanalytical spectrometer equipped with a motorized xy stage and autofocus. The spectra were generated with 17 mW, 632.8 nm He–Ne laser excitation and dispersed with the 1800 grooves/mm grating across the 0.8 m length of the spectrograph. The laser power was 4 mW at the sample surface. The spectral resolution is estimated to be less than 0.5 cm^{-1} for a slit width of 150 μm and a confocal hole of 300 μm. The crystal structures of the Li_xWO_3 layers in an operating EC device subjected to potentials of 1.0–2.5 V were measured by XRD. These measurements were carried out in reflection with a custom built theta-theta diffractometer equipped with pyrolytic graphite monochromator and analyzer crystals. Cu Kα radiation ($\lambda = 0.154178$ nm) was used for the measurements, and the data are shown as a function of the modulus of the scattering vector, $q = 4\pi\lambda^{-1}\sin\theta$ where 2θ is the scattering angle. Air scattering was avoided by evacuating the sample space. Two samples were measured: an empty ITO-coated glass substrate and a substrate with an m-WO_3 layer deposited on it. Subsequently, an EC device was assembled. It was colored and bleached by applying voltages ranging from 1.0 to 2.5 V. For these measurements, the ITO-coated-glass-2 slide was removed. The optical transmittance spectra of the EC devices in their colored/bleached states were recorded at normal incidence with a Biochrom Ultrospec 2000 UV-Visible spectrophotometer.

Results and discussions

Meso-/macroporous features

The textural features of the WO_3 layer prepared by using ORMOSIL templates and calcined at 500 °C were analyzed by SEM, TEM, and N_2 absorption isotherms.

SEM of the m-WO_3 layer

Figure 1a shows the SEM image of the WO_3 layer recorded at a tilt angle of 45°, displaying the planar features as well as the cross-sectional features of the deposited EC layer. The surface of the layer as observed from the planar features shows a large porosity with varying pore diameters. The cross-sectional view demonstrates that the pores are prevalent through the entire volume of the sample. When the sample is heat treated at 400 °C or above, the organic part of the ORMOSIL is removed from the entire volume

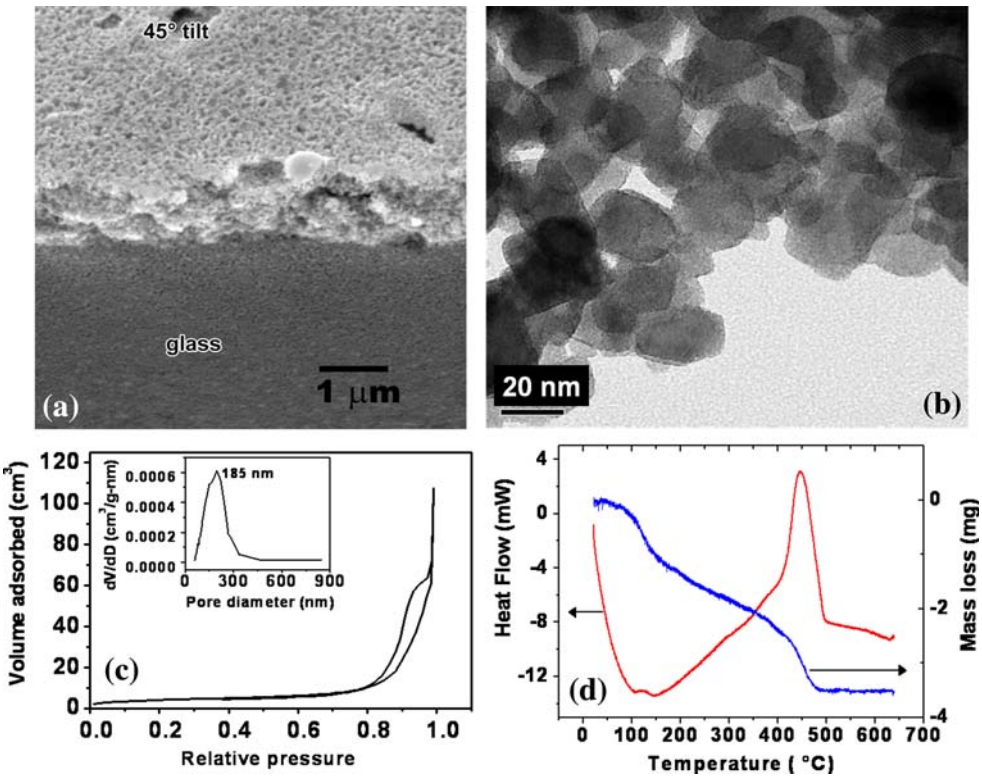

Fig. 1 **a** Scanning electron microscope (SEM) image of the m-WO_3 layer. **b** Transmission electron microscope image of the WO_3 layer. **c** N_2 absorption–desorption isotherms with pore size distribution shown in the inset. **d** TGA and the thermoanalysis of the as-prepared WO_3 sample

of the sample and a macroporous nanocrystalline WO_3 layer is formed.

TEM of the m-WO_3 layer

Figure 1b shows the TEM image of the WO_3 sample displaying mesoporous features. The pore sizes estimated from two random locations are 16.7 and 4.7 nm and are very well within the definition of mesoporous dimensions (2 and 50 nm). This indicates that the walls of macroporous domains have mesoporous features. The lattice spacings determined by the inverse Fourier transforms of the lattice fringes at two different points on the WO_3 crystallites (not shown here) were found to be 0.3658 and 0.3625 nm. This lattice spacing correlates very well with that of monoclinic WO_3 (m-WO_3). The average WO_3 crystallite size in the TEM image is 19.3 nm.

N_2 adsorption–desorption isotherm

The N_2 adsorption–desorption isotherm of the WO_3 sample annealed at 500 °C is presented in Fig. 1c. The isotherm of the sample is of classical type II, indicative of macroporosity according to the IUPAC. The pore size distribution curve obtained by the BJH method using the adsorption branch of the isotherm is broad, and is centered at about 185 nm. The BET surface area is found to be $\sim$150 m^2/g with a pore volume of 0.166 cm^3/g.

Thermogravimetric measurements

Figure 1d shows both the thermogravimetric analysis (TGA) and thermoanalysis of the as-prepared WO_3 sample. The as-prepared WO_3 sample is a mixture of amorphous hydrated tungsten oxide and ORMOSIL. Three different regions are seen. In the first region, up to 150 °C, the mass loss is attributed to the removal of water that is present in the as-prepared WO_3. The second region, from 150 to 400 °C, is attributed to the decomposition of the organic part of the ORMOSIL. The third region between 425 and 475 °C shows a sudden decrease in the mass of the sample, indicating a complete removal of the organic content. The thermoanalysis curve shows a high exothermic peak, indicating that all the organic contents are burnt away at the temperatures between 425 and 475 °C. There is no further loss of mass after 475 °C.

Structural analysis of EC layer

The crystalline structure of the WO_3 layer was studied by micro-Raman spectroscopy and XRD. Figure 2a shows the Raman spectrum of the WO_3 layer annealed at 500 °C. The Raman modes observed at 133.3 cm^{-1} is attributed to the lattice modes. The mode observed at 270.7 cm^{-1} is emerging from the O–W–O deformation vibration. The modes observed at 713.7 and 806.2 cm^{-1} are attributed to the O–W–O stretching vibrations. The modes observed in

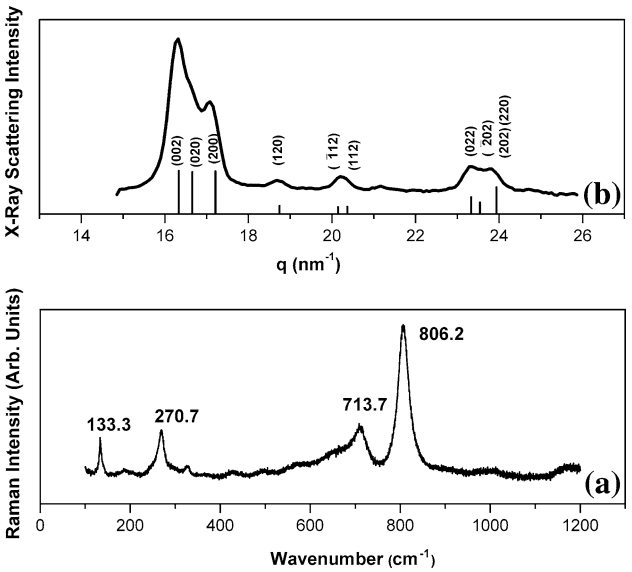

Fig. 2 Raman spectrum (**a**) and XRD pattern (**b**) of the m-WO_3 layer, indicating the monoclinic phase of tungsten oxide in m-WO_3 layer

the Raman spectra are the characteristic features of monoclinic WO_3 as reported by Daniel et al. [14]. Among these modes, the deformation vibration mode which is located at 270.7 cm^{-1} is red-shifted by 2.3 cm^{-1} when compared to the bulk m-WO_3, which appears at 273 cm^{-1} [14]. Boulova and Lucazeau have performed systematic studies on the Raman spectrum of nanocrystalline m-WO_3 and have observed that the deformation mode shows a systematic change in peak position from 263 to 275 cm^{-1} as the particle size increases from 4 to 60 nm [16]. With this precedence, the shift in the deformation mode is attributed to the nanocrystalline nature of the film.

The XRD pattern of the m-WO_3 layer is shown in Fig. 2b. The peak position observed in the XRD pattern matches very well with the m-WO_3 and indexed as reported in JCPDS 43-1035 [23]. The crystallite size obtained from the XRD is about 16.7 nm, which is in agreement with the TEM data presented above. Thus, Raman and XRD data clearly show the monoclinic nanocrystalline structure of the tungsten oxide in WO_3 layer.

Electrochromic analysis

Optical properties

Figure 3 shows the optical transmittance spectra of the m-WO_3-based EC device in bleached state and colored at potentials of +1.0, +1.5, +2.0, and +2.5 V. The device returned to the initial bleached state when the voltages were reversed. The inset shows the digital photographic image of the EC devices at the above-mentioned potentials. In the bleached state, the transmittance of the device at 1100 nm was 76.4%. At the coloration potentials of +1.0, +1.5, +2.0, and +2.5 V, the transmittance reduced to 43.5, 2.6, 0.3, and 0.0%, respectively. The device exhibits an optical modulation of 76.1%, which is exceptionally high for EC devices. This high optical modulation is attributed to meso-/macroporous nature of the m-WO_3 layer. When the coloration potentials of +1.5, +2.0, and +2.5 V are applied, the peak position of the transmittance curve is observed at 513.5, 488.5, and 449.5 nm and the FWHM for the curves are 379.0, 238.0, and 143.0 nm, respectively.

It is to be noted that the transmittance of the meso-/macroporous m-WO_3 layer is lower as seen from the transmittance spectrum (solid line). It is 17.0% at the wavelength of 470 nm and increases monotonically to 68.4% at 1100 nm. When ICL is smeared on the surface of this meso-/macroporous m-WO_3 layer, to construct the EC device, the transmittance increases sharply to 75.4% for the wavelength of 500.0 nm and remains the same (i.e., 76%) at 1100 nm. This change in the optical transmission is attributed to the scattering in the film due to the microstructure. Volume scattering is generally created due to the inhomogeneities in the refractive index of the film [24]. We have already seen that the pore sizes in the film are in the order of the wavelengths of the visible region of the transmission spectra. If the pores are filled with air, it creates a nonuniform distribution of the refractive index in the film. When the ICL is smeared, the pores are filled by high refractive index medium (refractive index of ICL = 1.425 at the wavelength of 589.0 nm and refractive index of WO_3 thin film prepared by thermal evaporation is 1.95 at 600 nm [25]), the ICL + WO_3 medium is optically homogenous, leading to the higher specular transmission. This observation also evidences the presence of macroporous features, in addition to the N_2 adsorption–desorption and SEM measurements.

XRD studies on the working EC device as a function of applied potentials

The X-ray scattering of the Li_xWO_3 layer is shown in Fig. 4 as a function of the applied voltage. The diffraction pattern of the m-WO_3 layer sample corresponds to monoclinic WO_3, for which the JCPDS pattern is shown by the vertical bars. Each of Fig. 4A, B′, C′, D′ show all the six peaks corresponding to the monoclinic phase and all the peaks are indexed as (002), (020), (200), (120), ($\bar{1}$12), and (112) from left to right. The effect of the insertion and extraction of lithium at different voltages can be seen as shifts of the diffraction peak positions and change in the intensity of the peak positions. We determine the lattice constants *a, b,* and *c* and the angle β of the monoclinic phase for different sample states by fitting the diffraction

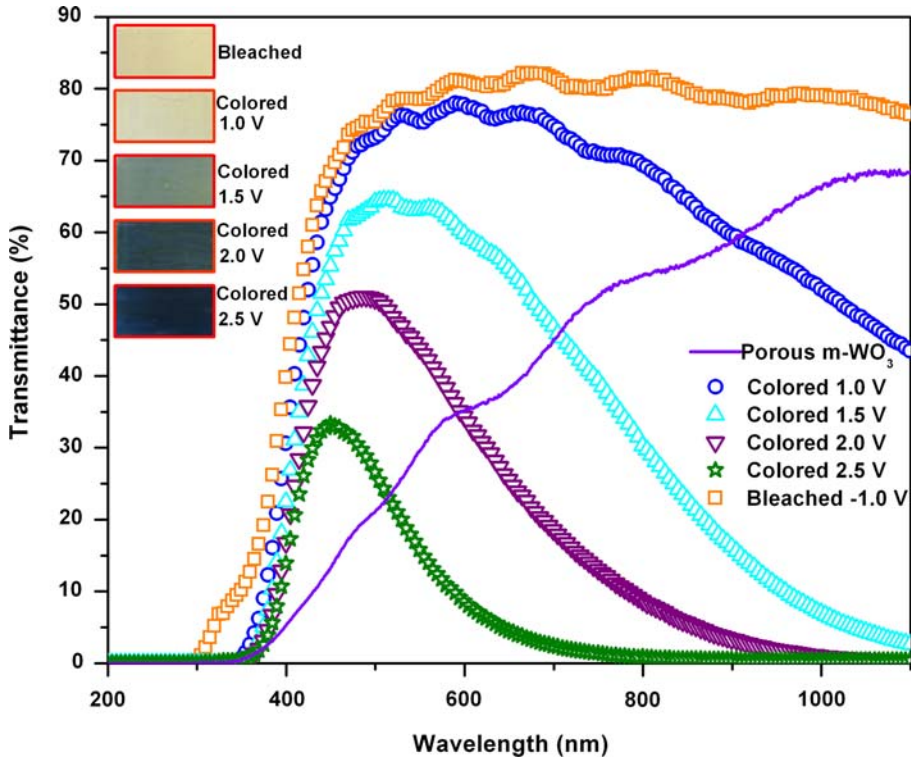

Fig. 3 Optical transmittance of the m-WO_3 layer colored at potentials of 1.0, 1.5, 2.0, and 2.5 V and bleached at −1.0 V. The *inset* shows the digital photograph of the device in the colored and bleached states

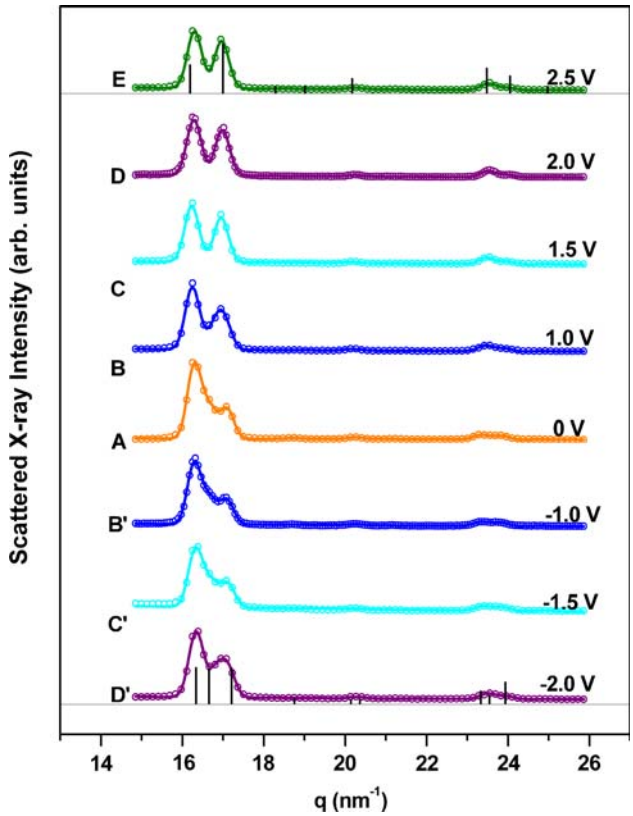

Fig. 4 XRD pattern of the device without any potential (*A*), colored at potentials of 1.0 V (*B*), 1.5 V (*C*), 2.0 V (*D*), and 2.5 V (*E*), and bleached at potentials of −1.0 V (*B′*), −1.5 V (*C′*), and −2.0 V (*D′*)

patterns shown in Fig. 4. Each spectrum is fitted to a series of Gaussian peaks superimposed on an overall quadratic background. These fits, shown as solid lines in Fig. 4, closely match the measured data (open circles). The peak width Δq, which is assumed to be the same for all reflections, is treated as a fitting parameter as well as the intensities of the individual peaks. We correct it for the instrument resolution and use it to estimate the crystallite size using the Scherrer method, assuming that, e.g., crystallite-to-crystallite variations of the lattice parameter do not contribute to the peak widths. The fitted lattice parameters and the crystallite sizes calculated based on the fitted peak widths are shown in Fig. 5 in the order of the measurement sequence, starting with the nonintercalated m-WO_3 layer. The voltage applied to the device prior to the measurement is indicated for each measurement. The positive potentials are the coloration potentials and negative potentials are the bleaching potentials.

It can be observed from Fig. 4 that as the coloration voltages were applied, the XRD peaks show a change in the position and in the intensities, indicating a structural change associated with intercalation of Li. The observed changes were quantified by measuring the plane and hence the lattice parameters and they are presented in Fig. 5. The XRD pattern of the m-WO_3 layer has the lattice parameter $a = 0.73512$ nm, $b = 0.75396$ nm, and $c = 0.77119$ nm. When the coloration potential of 1.0 V is applied, the lattice parameters a and b converge toward each other (i.e.,

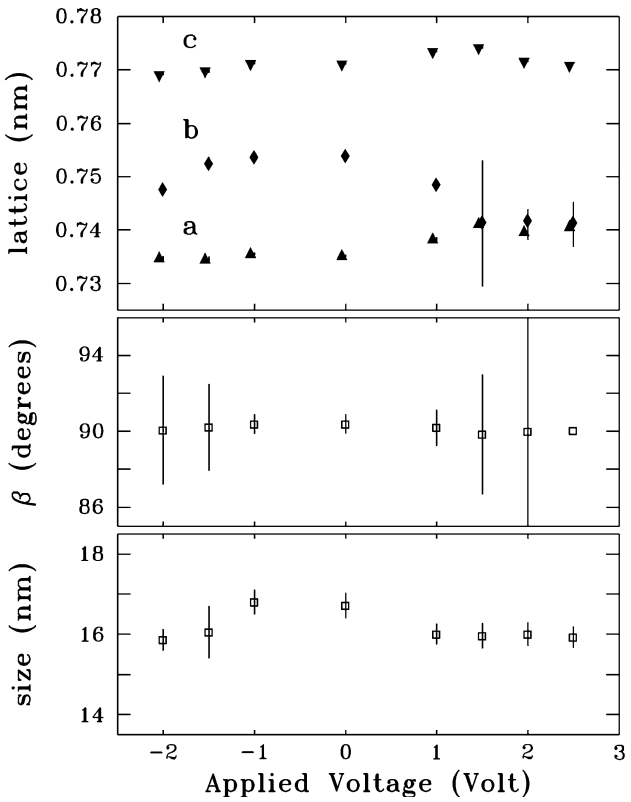

Fig. 5 Lattice parameter calculated from the XRD patterns of the device at various potentials (a), the angular parameter (b), and the crystallite sizes calculated from the XRD patterns of the device at various potentials using Scherer formula (c)

$a = 0.73825$ nm; $b = 0.74855$ nm) while lattice parameter c increases to 0.77346 nm. This indicates that Li intercalation at 1.0 V initiates a symmetry in the a–b plane. When the applied potential is increased to 1.5 V, the a and b lattice parameters completely converge to a value of $a = 0.7412$ and $b = 0.74148$ while parameter c is further increased to 0.77418. The XRD pattern of the Li_xWO_3 after Li intercalation at 1.5 V resembles that of the tetragonal WO_3 crystalline phase (JCPDS 89-1287) [23]. This observation demonstrates that the phase transition from m-WO_3 to t-Li_xWO_3 is complete at 1.5 V.

As the Li ion intercalation is performed at 2.0 and 2.5 V, the lattice parameter c decreases from its maximum value to $c = 0.77165$ nm, converging toward a and b. It is clear that the crystalline state of the Li_xWO_3 layers after intercalation of Li at 2.0 and 2.5 V is in the higher symmetry state above tetragonal phase. It should be noted that, a cubic phase has been observed when Li ions are intercalated into similarly prepared samples at an applied potential of 3.0 V [7]. This suggests that the convergence of the value of the lattice parameter c toward those of a and b is an indication of the motion of the system toward higher symmetric cubic phase. Hence, the observed crystalline Li_xWO_3 phase obtained at 2.0 and 2.5 V is an intermediate crystalline structure between tetragonal and cubic phases.

It should be noted that, when the Li ions are deintercalated by applying reverse potentials, the crystalline structure of m-WO3 layer reverts to the initial monoclinic lattice. This is shown in Fig. 4B, C, and D. In the XRD pattern shown in Fig. 4D, a complete deintercalation was not observed as the time of deintercalation ($\sim$300 s) was not sufficient, whereas Fig. 4B and C exhibits a complete Li deintercalation.

Raman studies on the working EC device as a function of applied potentials

Figure 6A shows the Raman spectrum of the m-WO_3 layer. The m-WO_3 features are observed from the Raman peaks at 133.3 cm^{-1} (lattice mode), 270.7 cm^{-1} δ(O–W–O), and ν(O–W–O) modes at 713.7 and 806.2 cm^{-1}. The Raman peaks at 713.7 and 806.2 cm^{-1} attributed to ν(O–W–O) modes of m-WO_3 were followed during the EC coloration and bleaching at applied potentials from −2.0 to 2.5 V.

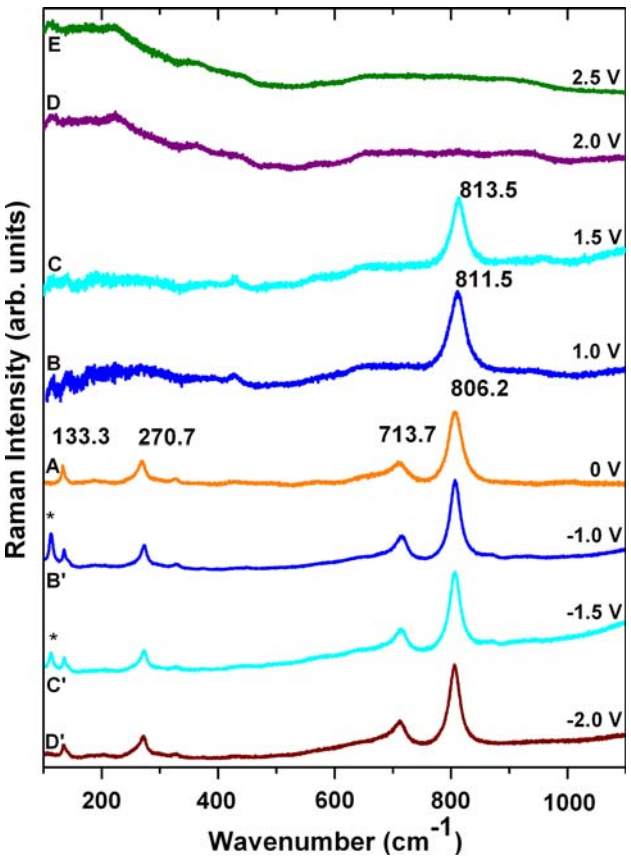

Fig. 6 Raman spectra of the device without any potential (*A*), colored at potentials of 1.0 V (*B*), 1.5 V (*C*), 2.0 V (*D*), and 2.5 V (*E*), and bleached at potentials of −1.0 V (*B′*), −1.5 V (*C′*), and −2.0 V (*D′*) (The Raman band at 113.3 cm^{-1} indicated by *asterisk* in *B′* and *C′* is emerging from the ICL)

The Raman spectrum of the m-WO_3 layer after Li was intercalated (Li_xWO_3) at a potential of 1.0 V is shown in the Fig. 6B. The ν(O–W–O) mode at 713.7 cm^{-1} vanished and the peak at 806.2 shifts to 811.5 cm^{-1}. The lower energy modes at 133.3 and 270.7 cm^{-1} also vanished completely. Figure 6C shows the Raman spectrum of Li_xWO_3 layer recorded after applying a potential of 1.5 V. A Raman band is seen at 813.5 cm^{-1} and the spectrum is similar to the Fig. 6B except for the blue shift in the peak position by 2 cm^{-1}.

To understand these spectral features, one needs to consider the structural modifications that are induced by the intercalation of Li. It is known that crystalline tungsten oxide when intercalated with protons or Li ions undergo phase transformations toward higher symmetrical states. Kuzmin et al. and Cazzanelli et al. have demonstrated that, in H_xWO_3, for the value of $0.1 < x < 0.23$, the m-WO_3 transforms to tetragonal WO_3 and the Raman spectra of tetragonal-H_xWO_3 is characterized by a single peak at 816 cm^{-1} [17, 19]. Lee et al. have studied the Li intercalation into m-WO_3 by performing a dry lithiation. They have observed that, for $x = 0.3$, Li_xWO_3 film exhibits only one peak that is observed at 806 cm^{-1}[20].

Recently, we have demonstrated that when Li was intercalated into a WO_3 layer having a mixed phase (monoclinic-WO_3 + hexagonal-WO_3), Raman spectrum on the resulting Li_xWO_3 layer showed a single peak at 811 cm^{-1}, corresponding to a value of $0.1 < x < 0.23$ [7]. In all the above-mentioned results, the resulting single Raman peak between 811 and 816 cm^{-1} has been attributed to the formation of higher symmetric tetragonal phase. From the Raman results shown in Fig. 6B and C, it is clear that the Li intercalation into the m-WO_3 layer leads to a phase transition toward higher symmetric state. To understand the observed phase changes, it is important to know the structure of m-WO_3 and tetragonal WO_3. The WO_6 octahedron in the m-WO_3 structure is constituted by three long and three short W–O bonds, whereas a tetragonal phase is characterized by the symmetric bonds in the *a–b* plane. When Li is intercalated into the m-WO_3 at an applied voltage of 1.0 V, one of the Raman bands that belong to O–W–O stretching of m-WO_3 vanishes and the other mode is shifted to 811.5 cm^{-1}. The XRD data on m-WO_3 film when intercalated with Li at an applied potential of 1.0 V indicates that the lattice parameters *a* and *b* comes closer to each other and parameter *c* increases. This scenario shows that this is the onset of the phase transformation toward t-Li_xWO_3. For an applied voltage of 1.5 V, the Raman spectrum of Li_xWO_3 layer shows a further shift to 813.5 cm^{-1} and XRD data indicates that lattice parameters *a* and *b* have converged to the same value ($a = 0.7412$ nm; $b = 0.74148$ nm) and lattice parameter *c* has increased further (0.77418 nm). This indicates that the phase transition to t-Li_xWO_3 is complete. This is also a clear demonstration of phase transition from m-WO_3 to tetragonal-Li_xWO_3 in nanocrystalline m-WO_3 layer.

Figure 6D and E shows the Raman spectra of the m-WO_3 layer, colored at potentials of 2.0 and 2.5 V. The Raman modes due to ν(O–W–O) vanish completely. It has been observed from the XRD of Li_xWO_3 layer, that for the applied potential of 1.5 V, the lattice parameter *c* attains a maximum value and for the applied potentials of 2.0 and 2.5 V, the lattice parameter *c* starts decreasing (i.e., $c = 0.77165$ nm at 2.0 V and $c = 0.77092$ nm at 2.5 V). At the same time, the lattice parameters *a* (= 0.73965 nm) and *b* (= 0.74178) converge to a same value within the error limit and they remain the same within the error limit. This tendency of the lattice parameter *c* to converge toward lattice parameter *a* and *b* indicates that the system is moving toward cubic phase as the amount of intercalated Li is increased. The vanishing of Raman mode is also attributed to this trend of Li_xWO_3 system to move toward cubic phase. It has been reported by Zhong et al. that the cubic Li_xWO_3 phase was obtained for $x > 0.5$ [21]. In our case, Li intercalation into WO_3 layer at 2.5 V shows that it has not reached the complete cubic phase, whereas a higher symmetric state than that of tetragonal phase is clearly observed. This indicates that for the applied potential of 2.0 and 2.5 V, the amount of Li that has intercalated into m-WO_3 is between 0.23 and 0.5. This is the first report that an intermediate crystalline state between tetragonal and cubic is observed in Li_xWO_3 system. The complete vanishing of ν(O–W–O) Raman modes observed at a coloration potentials of +2.0 and + 2.5 V is attributed to a phase transition to a higher symmetric state than that of t-Li_xWO_3. Thus, Raman spectroscopy is very sensitive even to a very small change in the lattice parameters as observed in this work. This clearly demonstrates that Raman spectroscopy can efficiently follow the Li intercalation into nanocrystalline m-WO_3, and is very successful in recording the intermediate states. Figure 6B′–D′ shows the Raman spectra of the m-WO_3 layer of the EC device after the deintercalation of Li at potentials of −1, −1.5, and −2.0 V. The recorded Raman spectra exhibit the spectral features as that of the initial m-WO_3 layer (Fig. 6A). This demonstrates the EC reversibility of the system, which can be efficiently followed by Raman spectroscopy. The obtained results are in excellent correlation to the optical study in which complete bleaching of the device was observed (Fig. 3).

Conclusions

Meso-/macrostructured WO_3 thin films were synthesized using tungstic acid as precursor and ORMOSIL as a

templating agent, after calcination at 500 °C. This heat treatment has resulted in nanocrystalline monoclinic tungsten oxide (m-WO_3) film with crystallite sizes of $\sim$16 nm, preserving the meso-/macroporous structure. An asymmetric transmissive EC device based on the meso-/macroporous m-WO_3 thin film was constructed. Coloration and bleaching of the EC device was achieved by intercalating and deintercalating Li into the WO_3-EC layer at applied potentials of $\pm$1.0, $\pm$1.5, $\pm$2.0, and +2.5 V. Detailed micro-Raman and XRD studies of the structural changes in Li_xWO_3 were performed during Li intercalation and deintercalation. Upon intercalation, the initially monoclinic WO_3 layer attains higher symmetry tetragonal phase (t-Li_xWO_3) at applied voltages up to 1.5 V. An intermediate higher symmetric state than that of t-Li_xWO_3, but lower than that of cubic c-Li_xWO_3, is observed at a coloration potentials of +2.0 and 2.5 V. All phases and phase transitions were identified both by Raman spectroscopy and XRD. Upon Li deintercalation, the observed phase transitions are reversed to initial m-WO_3. The optical transmission of the device was recorded in conjunction with Raman and XRD studies. The device exhibits an optical modulation of 76.1%, which is exceptionally high for EC devices. This high optical modulation is attributed to meso-/macroporous nature of the m-WO_3 layer. Furthermore, the optical modulation as a function of the applied potential demonstrates the functionality of this device for EC smart window applications.

Acknowledgements The financial support of the Research Assistantships Initiative of New Brunswick Innovation Fund (NBIF), the Atlantic Innovation Fund (AIF—Round II), and National Science and Engineering Research Council (NSERC) of Canada is gratefully acknowledged. We thank Dr. Louise Weaver (Microscopy Microanalysis Facility, University of New Brunswick, Fredericton, NB, Canada) for the TEM measurements, and Zoulika Hadj—Sadok (Laboratoire de Chimie des matériaux inorganiques – FUNDP, Namur, Belgique) for BET and thermogravimetric measurements.

References

1. Granqvist CG (1995) Handbook of inorganic electrochromic materials. Elsevier, New York
2. Granqvist CG (2000) Sol Energy Mater Sol Cells 60:201
3. Somani PR, Radhakrishnan S (2003) Mater Chem Phys 77:117
4. Deb SK (2008) Sol Energy Mater Sol Cells 92:245
5. Granqvist CG (2006) Nat Mater 5:89
6. Niklasson GA, Granqvist CG (2007) J Mater Chem 17:127
7. Balaji S, Albert A-S, Djaoued Y, Brüning R (2009) J Raman Spectrosc 40:92
8. Gogova D, Gesheva K, Szekeres A, Sendova-Vassileva M (1999) Phys Status Solidi A 176:969
9. Djaoued Y, Priya S, Balaji S (2008) J Non-Cryst Solids 354:673
10. Djaoued Y, Ashrit PV, Badilsecu S, Brüning R (2003) J Sol-Gel Sci Technol 28:235
11. Yang B, Li H, Blackford M, Luca V (2006) Curr Appl Phys 6:436
12. Opara Krašovec U, Georg A, Georg A, Wittwer V, Joachim L, Topič M (2004) Sol Energy Mater Sol Cells 84:369
13. Cheng W, Baudrin E, Dunn B, Zink JI (2001) J Mater Chem 11:92
14. Daniel MF, Desbat B, Lassegues JC (1987) J Solid State Chem 67:235
15. Boulova M, Rosman M, Bouvier P, Lucazeau G (2002) J Phys Condens Matter 14:5849
16. Boulova M, Lucazeau G (2002) J Solid State Chem 167:425
17. Kuzmin A, Purans J, Cazznelli E, Vinegoni C, Mariotti G (1998) J Appl Phys 84:5515
18. Pyper O, Kaschner A, Thomsen C (2002) Sol Energy Mater Sol Cells 71:511
19. Cazznelli E, Vinegoni C, Mariotto G, Kuzmin A, Purans J (1999) J Solid State Chem 143:24
20. Lee S-H, Seong MJ, Cheong HM, Ozkan E, Tracy EC, Deb SK (2003) Solid State Ionics 156:447
21. Zhong Q, Dahn JR, Colbow K (1992) Phys Rev B 46:2554
22. Stathatos E, Lianos P, Štangar UL, Orel B (2002) Adv Mater 14:354
23. Powder Diffraction Files Inorganic and Organic (Cards No: 43-1035 (Monoclinic-WO_3), No: 89-1287 (tetragonal-WO_3)) (1996) JCPDS-International Centre for Diffraction Data, PDF2 Data Base, Swarthmore
24. Amra C (1992) Appl Opt 32:5481
25. Von Rottkay K, Rubin M, Wen S-J (1997) Thin Solid Films 306:10